Mixing layer instability and vorticity amplification in a creeping viscoelastic flow

Atul Varshney[1,2] and Victor Steinberg[1,3]
[1]*Department of Physics of Complex Systems, Weizmann Institute of Science, Rehovot 76100, Israel*
[2]*Institute of Science and Technology Austria, Am Campus 1, 3400 Klosterneuburg, Austria*
[3]*The Racah Institute of Physics, Hebrew University of Jerusalem, Jerusalem 91904, Israel*

(Received 1 February 2018; published 16 October 2018)

We report quantitative evidence of mixing-layer elastic instability in a viscoelastic fluid flow between two widely spaced obstacles hindering a channel flow at $\mathrm{Re} \ll 1$ and $\mathrm{Wi} \gg 1$. Two mixing layers with nonuniform shear velocity profiles are formed in the region between the obstacles. The mixing-layer instability arises in the vicinity of an inflection point on the shear velocity profile with a steep variation in the elastic stress. The instability results in an intermittent appearance of small vortices in the mixing layers and an amplification of spatiotemporal averaged vorticity in the elastic turbulence regime. The latter is characterized through scaling of friction factor with Wi and both pressure and velocity spectra. Furthermore, the observations reported provide improved understanding of the stability of the mixing layer in a viscoelastic fluid at large elasticity, i.e., $\mathrm{Wi} \gg 1$ and $\mathrm{Re} \ll 1$ and oppose the current view of suppression of vorticity solely by polymer additives.

DOI: 10.1103/PhysRevFluids.3.103303

I. INTRODUCTION

Instability of a parallel shear flow of Newtonian fluid in different flow geometries and for various shear velocity profiles, particularly in connection to the transition to turbulence, was a subject of extensive investigation for about 150 years since the first studies of Kelvin and Helmholtz [1–3]. A subclass of such flows, namely free shear flows, includes jets, wakes, and mixing layers. The simplest of them is the mixing layer—a layer between two uniform fluid streams with boundaries located far away—which is distinguished by a nonlinear shear velocity profile with an inflection point [1–3]. At moderate Reynolds number Re, the mixing layer becomes unstable due to Kelvin-Helmholtz (KH) instability, resulting in a vortex chain—classical example of the vortex generation in otherwise irrotational flow [1–5]. A further increase of Re results in vorticity amplification due to vortex stretching by a velocity gradient, the main mechanism of the vorticity enhancement in Newtonian fluid flow [4,5]. Moreover, it is shown that the KH instability of the free shear layer plays a key role in a self-sustained process in transition to turbulence in pipe, channel, and plane Couette flows, where the original streamwise rolls supply energy to a streak flow that becomes unstable due to the KH instability, re-energizing the original streamwise rolls [6].

In viscoelastic fluids, the role of elastic stress, generated by polymers stretching in a shear flow, in the stability of the free shear layer was investigated experimentally as well as theoretically mostly at large Reynolds (Re) and Weissenberg numbers (Wi) and at low polymer concentrations [7]. Here, Wi defines a degree of polymer stretching. A general conclusion is drawn from studies prior to 1990s that no pure elastic instabilities exist in the parallel shear viscoelastic flows [8]. The first stability analysis of a viscoelastic fluid planar mixing layer, formed by two fluid streams moving with equal speeds in opposite directions, shows that the elastic stress has a stabilizing effect for $\mathrm{Re} \gg 1$ and $\mathrm{Wi} \gg 1$ [9], in agreement with the results of early experimental studies [10,11]. In an

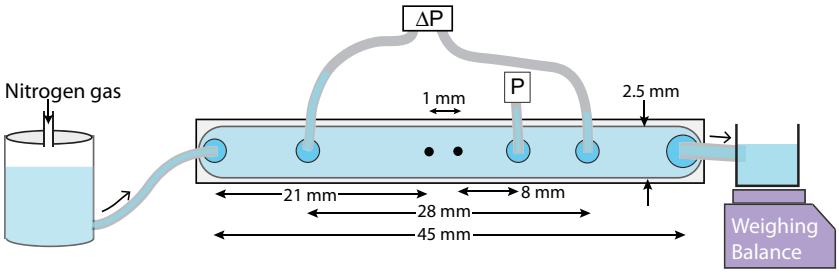

FIG. 1. Schematic of experimental setup (not to scale).

insightful theoretical study, Hinch considered an elastic membrane between two counterpropagating Newtonian fluid streams, similar to two-fluid Newtonian streams with surface tension at the interface (see Appendix in Ref. [9]). It was found that the inertial instability of a Newtonian mixing layer is stabilized by a surge in elastic stresses across the interface for high elasticity ($El = \mathrm{Wi}/\mathrm{Re}$). In the elastic fluid, polymers stretched by a shear flow form an elastic membrane that resists bending. For small nonzero elasticity, an instability driven by a discontinuity in the normal elastic stress was reported [12]. Further, a suppression of the inertial instability by elasticity in the mixing layer of a polymer solution was confirmed by experiments on tunnel flow with a sudden large backward-facing step, where a delay in the formation of large-scale structures is observed [13], as well as in wakes [14–16] at $\mathrm{Re} \gg 1$ and $\mathrm{Wi} \gg 1$. However, a recent study extended to spatially developing mixing layers [17] reveals, in contrast, the destabilizing effect of elastic stress at moderate values of El, while at large El the flow is stabilized in accordance with Ref. [9]. Moreover, these results ruled out the occurrence of a pure elastic instability in free shear flows.

Here, we concern with a pure elastic instability of the mixing layer at $\mathrm{Re} \ll 1$ and $\mathrm{Wi} \gg 1$, i.e., an elastic analog of the Kelvin-Helmholtz instability in viscoelastic creeping flows. To the best of our knowledge, theoretical as well as experimental studies are lacking in the literature on this subject. However, very recent numerical studies, still unpublished, show a generic pure elastic instability of the mixing layer with a hyperbolic tangent shear velocity profile leading to a large jump in the elastic stress [18,19], similar to that investigated in Ref. [9] but conducted at $\mathrm{Re} \ll 1$ and $\mathrm{Wi} \gg 1$. Moreover, at $\mathrm{Re} \gg 1$ the numerical results in Refs. [18,19] confirm the conclusion of Ref. [9] that elasticity stabilizes the mixing layer, while at $\mathrm{Re} \ll 1$ and fixed $\mathrm{Wi} \gg 1$, the new pure elastic instability leads to a generation of a vortex chain state. As indicated in Ref. [19], the elastic KH instability could be a generic mechanism in a self-sustained process in transition to elastic turbulence in channel and plane Couette flows at $\mathrm{Wi} \gg 1$ and $\mathrm{Re} \ll 1$ [20], similar to that found and analyzed for Newtonian fluid at $\mathrm{Re} \gg 1$ [6].

In this paper, we report quantitative evidence of elastic instability of two mixing layers in a viscoelastic fluid between two widely spaced obstacles hindering the channel flow at $\mathrm{Re} \ll 1$ and $\mathrm{Wi} \gg 1$. The instability results in the generation of small-size vortices and vorticity enhancement by elastic stress in absence of inertia. The two mixing layers with nonuniform shear velocity profiles $u(y)$ are generated by a pair of counter-rotating elongated vortices that fill the space between two obstacles in length and width. The latter results from the instability causing an increase of the vortex length with Wi at a preserved streamline curvature [21]. We characterize the circulation of the small vortices and its dependence on Wi, transition to elastic turbulence (ET), and ET properties [22–24] by measuring the friction factor, the average vorticity growth, and frequency power spectra of both velocity and pressure fluctuations as a function of Wi.

II. EXPERIMENTAL SETUP

The experiments are conducted in a linear channel of dimension $L \times w \times h = 45 \times 2.5 \times 1\,\mathrm{mm}^3$, shown schematically in Fig. 1. The fluid flow is hindered by two cylindrical obstacles of

diameter $2R = 0.30$ mm made of stainless steel separated by a distance $e = 1$ mm and located at the center of the channel. Thus, the geometrical parameters of the device are $2R/w = 0.12$, $h/w = 0.4$, and $e/2R = 3.3$ (see Fig. 1). The channel is prepared from transparent acrylic glass, Polymethyl methacrylate (PMMA). The fluid is driven by N_2 gas at a pressure up to $\approx$10 psi and injected via the inlet into a rectangular channel. As a working fluid, a dilute polymer solution of high-molecular-weight polyacrylamide (PAAm, $M_w = 18$ MDa; Polysciences) at concentration $c = 80$ ppm ($c/c^* \simeq 0.4$, where $c^* = 200$ ppm is the overlap concentration for the polymer used [25]), is prepared in a viscous solvent of 60% sucrose and 1% NaCl by weight. The solvent viscosity, η_s, at 20°C is measured in a commercial rheometer (AR-1000; TA Instruments) to be 0.1 Pa s. Addition of the polymer to the solvent increases the solution viscosity, η, up to 0.13 Pa s. The stress-relaxation method [25] is employed to obtain longest relaxation time of the polymer solution, $\lambda = 10 \pm 0.5$ s.

A differential pressure sensor (HSC series, Honeywell) measures the pressure drop ΔP across the obstacles and an additional absolute pressure sensor (ABP series, Honeywell) records the pressure P fluctuations after the downstream cylinder, as shown schematically in Fig. 1. The fluid exiting the channel outlet is weighed instantaneously $W(t)$ as a function of time t by a PC-interfaced balance (BA210S, Sartorius) with a sampling rate of 5 Hz and a resolution of 0.1 mg. The time-averaged fluid discharge rate $\bar{Q}$ is estimated as $\overline{\Delta W/\Delta t}$. Thus, Weissenberg and Reynolds numbers are defined as $\mathrm{Wi} = \lambda\bar{u}/2R$ and $\mathrm{Re} = 2R\bar{u}\rho/\eta$, respectively; here $\bar{u} = \bar{Q}/\rho wh$ and fluid density $\rho = 1286$ Kg/m^3. For flow visualization, the solution is seeded with fluorescent particles of diameter 1 μm (Fluoresbrite YG, Polysciences). The region between the obstacles is imaged in the midplane via a microscope (Olympus IX70), illuminated uniformly with LED (Luxeon Rebel) at 447.5 nm wavelength, and a CCD camera (GX1920; Prosilica) attached to the microscope records about 5000 images of a spatial resolution 1936×1456 pixels at a rate of 50 fps. To conduct particle image velocimetry (μPIV) with high spatially resolved velocity measurements, a CMOS camera (MC124MG-SY with Sony sensor IMX253; XIMEA) is used to record 600 frames with a spatial resolution of 4112×3008 pixels and 8-bits grayscale resolution at a rate of 35 fps that allows us to obtain the spatially resolved velocity field $\vec{U} = (u, v)$ of 5×5 μm^2 with 50% overlap in the region between the cylinders for a chosen interrogation window 32×32 pixel^2 [26].

III. RESULTS

Various flow regimes are explored in the experiment up to maximum values of $\mathrm{Wi}_{\max} \simeq 184$ and $\mathrm{Re}_{\max} \simeq 0.02$. Inset in Fig. 2 shows the dependence of the friction factor versus Wi, and the main plot in Fig. 2 presents the normalized friction factor f/f_{lam} as a function of Wi, where $f = 2D_h\Delta P/\rho\bar{u}^2L_c$ is the friction factor, $D_h = 2wh/(w+h) = 1.43$ mm is the hydraulic radius, and $L_c = 28$ mm is the distance between the tubes to measure the pressure drop in the channel (see Fig. 1). Above the elastic instability at $\mathrm{Wi}_{c1} \simeq 12$ and up to $\mathrm{Wi} \approx 30$, f/f_{lam} grows with power-law $\mathrm{Wi}^{0.5}$ that has been discussed in Refs. [21,27], and another scaling region commencing at $\mathrm{Wi}_{c2} \approx 45$ is characterized by scaling $f/f_{\mathrm{lam}} \sim \mathrm{Wi}^{0.2}$. These two scaling regions are separated by a transition region between $\sim 30 \leqslant \mathrm{Wi} \leqslant 45$ marked by the gray band, where f/f_{lam} reduces. Figure 3 shows the Wi dependence of the spatial (region between the obstacles) and time ($\approx$100 s) averaged vorticity $\bar{\omega}$. At $\mathrm{Wi}_{c1} < \mathrm{Wi} < 30$, the power-law increase of $\bar{\omega}$ as $\mathrm{Wi}^{0.5}$ above the forward bifurcation occurs due to the growth of two elongated counter-rotating vortices, as reported in Ref. [21]. In the transition region at $30 \leqslant \mathrm{Wi} \leqslant \mathrm{Wi}_{c2} = 45$, $\bar{\omega}$ slightly reduces, and at $\mathrm{Wi} > \mathrm{Wi}_{c2}$ the $\bar{\omega}$ grows as $\mathrm{Wi}^{0.2}$ (see Fig. 3). The frequency power spectra of the cross-stream velocity v, taken at the location $(x/R, y/R) = (4.53, 0.14)$, exhibits power-law decay with an exponent $\alpha \approx -3.4 \pm 0.1$ (bottom inset in Fig. 3) at higher frequencies ν and at $\mathrm{Wi} > \mathrm{Wi}_{c2}$, characteristic to ET [24]. The frequency power spectra of the pressure fluctuations $S(P)$ in the same range of Wi show scaling behavior $S(P) \sim \nu^{\beta}$, where $\beta \approx -3.2 \pm 0.2$ (bottom inset in Fig. 2), which is also typical to the ET flow [28–30]. Moreover, at lower frequencies wide pronounced peaks in $S(v)$ are manifested at higher Wi that indicates either noisy oscillations or wave propagation accompanied ET (top inset in Fig. 3).

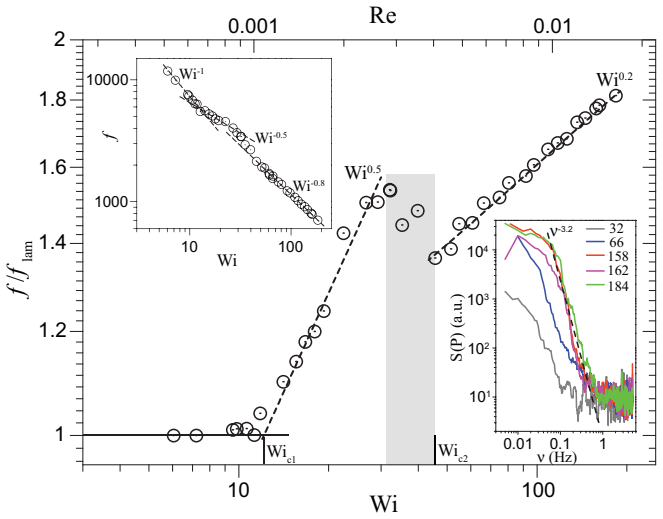

FIG. 2. Normalized friction factor $f/f_{\rm lam}$ vs Wi with the fits marked by dash lines above the first instability $f\mathrm{Wi} \sim \mathrm{Wi}^{0.5}$ and in the ET regime $f\mathrm{Wi} \sim \mathrm{Wi}^{0.2}$, which yield critical values for for respective transitions $\mathrm{Wi}_{c1} \simeq 12$ and $\mathrm{Wi}_{c2} \approx 45$. Gray band indicates the transition region. Top inset: Friction factor f versus Wi. Laminar flow is represented by scaling $f_{\rm lam} \sim \mathrm{Wi}^{-1}$. Bottom inset: Frequency power spectra of pressure fluctuations $S(P)$ in log-log coordinates for several Wi values. Dashed line indicates the power spectra decay with an exponent $\beta \approx -3.2 \pm 0.2$ in the ET regime.

To further illustrate the flow, snapshots of streak visualization averaged for ≈0.5 s are shown in Figs. 1SM, 2SM, and 3SM at $\mathrm{Wi} = 40,\ 158$, and 184, respectively, and also depicted through movies in the Supplemental Material [31], where small, about 40- to 60-μm-size vortices can be

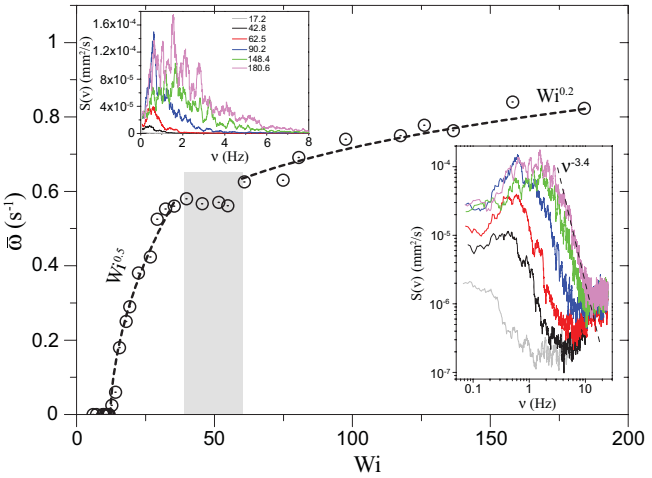

FIG. 3. Spatially and time-averaged vorticity $\bar{\omega}$ vs Wi with the fits by dashed lines $\bar{\omega} \sim \mathrm{Wi}^{0.5}$, and $\bar{\omega} \sim \mathrm{Wi}^{0.2}$. The gray band indicates the transition region of small vortex generation. Top inset: Frequency power spectra of cross-stream velocity, $S(v)$, for several Wi shown in linear coordinates. Bottom inset: $S(v)$ in log-log presentation for the same Wi. Dashed line indicates the power spectra decay with an exponent $\alpha \approx -3.4 \pm 0.1$ in the ET regime.

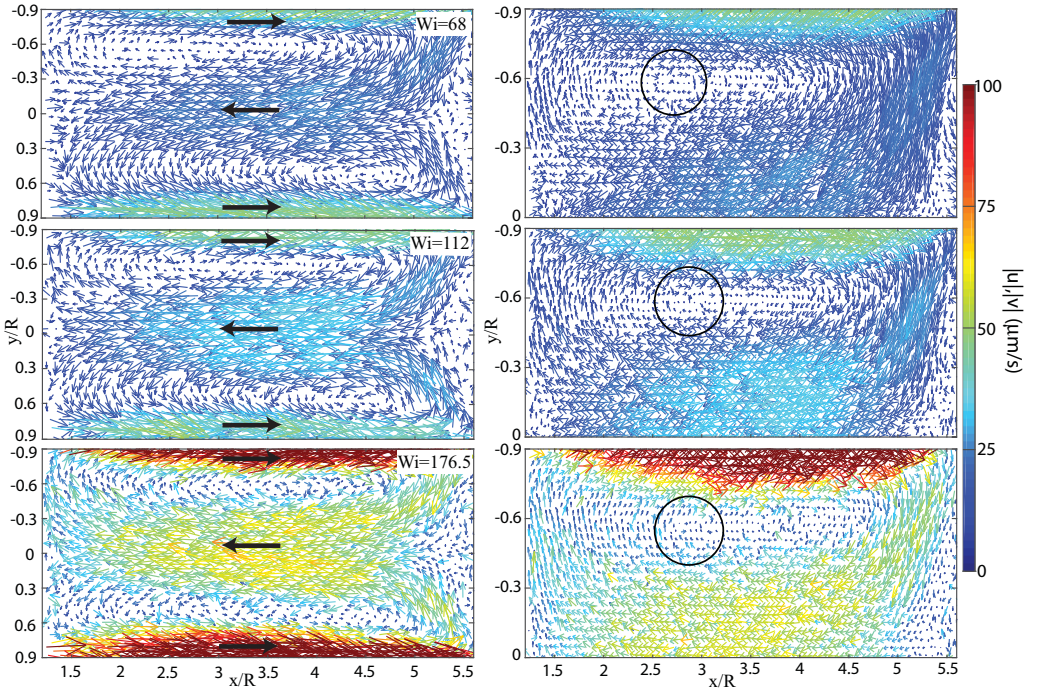

FIG. 4. Velocity fields between two obstacles at low (left-panel) and high (right-panel) magnifications for three values of Wi. The fields are obtained from μPIV and averaged over $\approx$1 s. Black arrows in left panel indicate the flow direction. Black circles in right panel highlight small vortex regions that are used for circulation calculation.

clearly identified. First, one notices the presence of two (upper and lower) shear layers, where small vortices are located closer to a separatrix between inner and outer flow regions. Second, in the ET regime rare and strong bursts of perturbations originated at the inner surface of the downstream obstacle can be observed (see movie 3 and a sequence of the snapshots in Fig. 3SM in the Supplemental Material [31]). A probable reason for these bursts may be overshooting of elastic stresses due to further stretching of polymers on curvilinear trajectories of the reverse flow.

Figure 4 shows velocity fields, time averaged $\approx$1 s, between two obstacles at low (left panel) and high (right panel) magnifications for three values of Wi. In high-magnification velocity field, one can identify small vortices and one of the vortices for each Wi is marked by a circle. One finds that vortices are located more on the right side, closer to the downstream obstacle. Because of the dynamical nature of the velocity field, intermittent strong bursts wash out the vortex structures and consequently the number of small vortices fluctuates on the timescale of these bursts of $\tau_b \approx 1$ s. However, a long time averaging ($\approx$100 s) of velocity field shows a smooth two large vortex structure without any appearance of small vortices. Moreover, it is important to emphasize that the divergence of velocity field, i.e., $\nabla \cdot \vec{U}(x, y)$ fluctuates near zero in the whole region between the obstacles (see Fig. 4SM in the Supplemental Material [31] at Wi = 176.5), which suggests the two-dimensional nature of the vortex flow.

The small vortices are quantified through a calculation of the circulation $\Gamma = \oint_C u_t ds$, where u_t is the azimuthal component of the velocity $\vec{U}$ integrated along a circle C. Figure 5 shows the dependence of Γ on the circle radius for three values of Wi. As expected for an isolated vortex, $|\Gamma|$ grows with radius of a circle, on which the integration occurs, and then saturates at the radius value that depends on Wi. If an isolated vortex exists in uniform flow, $|\Gamma|$ first saturates and then reduces

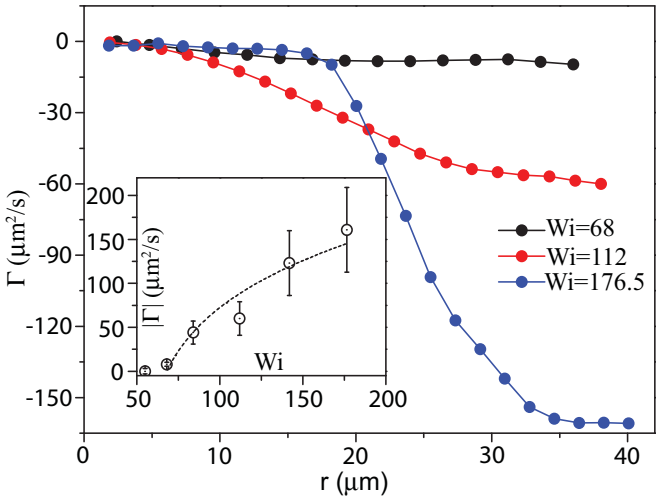

FIG. 5. Radial dependence of circulation Γ for three values of Wi. Inset: variation of $|\Gamma|$ with Wi. The dashed line is a fit $|\Gamma| \sim (\mathrm{Wi} - 55)^{0.2\pm0.05}$ to the data.

with further increasing of integration radius, whereas for a vortex in a shear flow after the saturation $|\Gamma|$ should increase due to the integration on the vorticity component of the shear. Indeed, this behavior is observed at further increase of the integration radius (see Fig. 5SM in the Supplemental Material [31]). Finally, in the inset of Fig. 5, the saturated value of $|\Gamma|$ is plotted as a function of Wi that indicates the onset of the small vortex generation at $\mathrm{Wi} = 55 \pm 12$ ($\approx \mathrm{Wi}_{c2}$) and shows above the onset a scaling behavior of the circulation (and so the vorticity) as $|\Gamma| \sim \mathrm{Wi}^{0.2}$.

IV. DISCUSSION

The main message delivered by the data is the onset of the generation of small vortices inside two mixing layers at $\mathrm{Wi} \approx \mathrm{Wi}_{c2}$ in the ET regime and their number fluctuates on the timescale τ_b of the occurrence of strong bursts. The circulation (and so the vorticity) of small individual vortices increases as $|\Gamma| \approx (\mathrm{Wi} - 55)^{0.2}$ (inset in Fig. 5), similar to the growth of the spatiotemporal averaged vorticity $\bar{\omega}$ of the large vortex in the ET regime (see Fig. 3). Thus, one observes three different regimes of $\bar{\omega}$ (Fig. 3) in the wake of a viscoelastic creeping flow between two widely spaced obstacles hindering the channel flow: (i) growth of $\bar{\omega}$ as $\mathrm{Wi}^{0.5}$ due to the increase of the vortex length at $\mathrm{Wi} > \mathrm{Wi}_{c1}$ above the elastic instability [21], (ii) slight reduction of $\bar{\omega}$ in the transition region, and (iii) growth of $\bar{\omega}$ as $\mathrm{Wi}^{0.2}$ in ET. The latter may be associated with the growth of the circulation (and so the vorticity) of each individual small vortex with the similar scaling.

Similar to the variation of $\bar{\omega}$ with Wi, one finds three different regimes of the dependence of f/f_{lam} on Wi (see Fig. 2). A growth of f/f_{lam} as $\mathrm{Wi}^{0.5}$ at $\mathrm{Wi} > \mathrm{Wi}_{c1}$ above the elastic instability [21]. In the transition region f/f_{lam} reduces with Wi, whereas the ET regime is characterized by the power-law dependence $f/f_{\mathrm{lam}} \sim \mathrm{Wi}^{0.2}$. It may suggest that the $\bar{\omega}$ growth in the ET regime is the main cause for the increase of f/f_{lam}. Moreover, the variations of $\bar{\omega}$ and f/f_{lam} are correlated in the whole range of Wi from Wi_{c1} and up to $\mathrm{Wi}_{\mathrm{max}}$ reached in the current study. An additional feature is the pronounced peaks at low frequencies in the velocity power spectra $S(v)$ indicating the presence of either oscillatory or wavy modes interacting with the vortices (see top inset in Fig. 3). On the other hand, the scaling exponents of the velocity $\alpha \simeq -3.4$ and the pressure fluctuations $\beta \simeq -3.2$ power spectra at high ν provide a firm evidence of the ET regime [22–24,32].

A natural question arises what can be the reason for the generation of the small vortices at $\mathrm{Wi} > \mathrm{Wi}_{c2}$ in the ET regime, what is a possible vorticity amplification mechanism in the ET regime

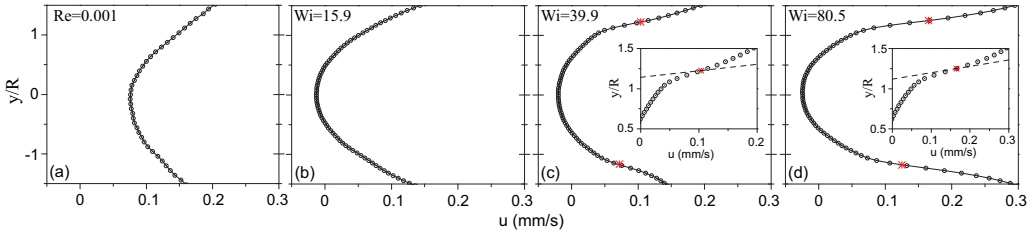

FIG. 6. Streamwise velocity profile $u(y)$ for (a) Newtonian solvent and [(b)–(d)] polymer solution at three Wi values. Red symbols in panels (c) and (d) indicate the inflection points on the profiles. Insets in panels (c) and (d) show the positions of inflection points in details; dashed line is a tangent at the inflection point. Noticeably, the velocity profile just above the first instability at $\mathrm{Wi} = 15.9$ is similar to that in the laminar region of a Newtonian solvent.

and what is so unique in this flow configuration compared to other flow geometries, where ET was observed and investigated but the vorticity generation was not found [22–24,33,34]. In a mixing layer of a Newtonian fluid, the presence of the inflection point in a streamwise shear velocity profile is the necessary condition for KH instability, called the Rayleigh criterion, and the inertia-driven KH instability of a mixing layer resulted in the generation of the vortex chain was theoretically understood and observed in experiments as well [1–3]. In the case of pure elastic instability, the presence of the inflection point in the nonuniform shear velocity profile suggests a steep variation in the elastic stress that may engender elastic instability, resulting in the vortices generation. Indeed at $\mathrm{Wi} \lesssim 40$, a streamwise velocity $u(y/R)$ has a parabolic profile, whereas at $\mathrm{Wi} \gtrsim 40$, two symmetrical inflection points on $u(y/R)$ for each mixing layer are observed (see Fig. 6 and also sketch in Fig. 7). Thus the key question is whether a mixing layer of a viscoelastic fluid at $\mathrm{Re} \ll 1$ and $\mathrm{Wi} \gg 1$ with a nonuniform shear velocity profile containing an inflection point can be so elastically unstable that it results in the vortex generation. Perhaps it could be addressed through numerical simulations performed in this parameter regime and for the similar flow configuration.

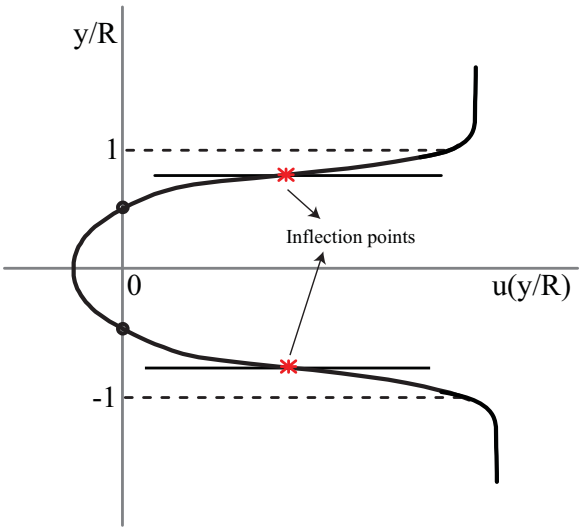

FIG. 7. Illustration of full streamwise velocity profile $u(y/R)$ in the inner and outer regions of the obstacles to demonstrate a similarity with two mixing layers. Red symbols are inflection points on the profile and solid lines are tangents at the inflection points.

V. CONCLUSION

Two key findings on the elastic instability of the mixing layer of a viscoelastic fluid at Re $\ll 1$ and Wi $\gg 1$ are described. The observations are reminiscent of the Kelvin-Helmholtz instability of the mixing layer in a Newtonian fluid at Re $\gg 1$ [1–3], namely, (i) the vortex generation in two mixing layers in a viscoelastic fluid between two obstacles hindering the channel flow at Re $\ll 1$ and Wi $\gg 1$, and (ii) the amplification of spatiotemporal averaged vorticity $\bar{\omega}$ and increase of the circulation $|\Gamma|$ of individual small vortices due to elastic stresses in the ET regime. Both observations provide a better understanding of the stability of shear flow of viscoelastic fluid at Wi $\gg 1$, $Re \ll 1$ and $El \gg 1$ [8,9,12] and in contrast with a well-known results that an injection of polymer additives into a Newtonian fluid flow inhibits vorticity [14–16] at Wi $\gg 1$, Re $\gg 1$. Recent numerical studies, though unpublished, conducted at Wi $\gg 1$ and Re $\ll 1$ reveal a generic purely elastic instability in a mixing layer of a viscoelastic fluid with a hyperbolic tangent shear velocity profile leading to a large jump in the elastic stress and generation of a vortex chain [18,19], similar to the KH instability in a mixing layer of a Newtonian fluid. In regard to the second finding, the mechanism of the vorticity enhancement by an elastic stress was suggested in Ref. [35] and may be relevant to explain the second paradox. The recent theoretical and numerical studies reveal that the elastic stress is also capable of amplifying a spanwise vorticity in a homogeneous viscoelastic shear flow particularly at $El \gg 1$. Moreover, the polymer torque resulting from the elastic stress is amplified as vorticity perturbations become aligned with the shear [35].

ACKNOWLEDGMENTS

V.S. is grateful for illuminating discussions with V. Lebedev and A. Morozov. We thank Guy Han and Yuri Burnishev for technical support. A.V. acknowledges support from the European Union's Horizon 2020 research and innovation programme under the Marie Skłodowska-Curie Grant Agreement No. 754411. This work was partially supported by the Israel Science Foundation (ISF; Grant No. 882/15) and the Binational USA-Israel Foundation (BSF; Grant No. 2016145).

[1] G. K. Batchelor, *An Introduction to Fluid Dynamics* (Cambridge University Press, Cambridge, UK, 1967).
[2] P. G. Drazin and W. H. Reid, *Hydrodynamic Stability* (Cambridge University Press, New York, 1982).
[3] P. K. Kundu and I. M. Cohen, *Fluid Mechanics*, 4th ed. (Elsevier, New York, 2008).
[4] P. G. Saffman, *Vortex Dynamics* (Cambridge University Press, New York, 1992).
[5] L. Landau and E. Lifshitz, *Fluid Mechanics* (Pergamon, London, 1959).
[6] F. Waleffe, Exact coherent structures in channel flow, J. Fluid Mech. **435**, 93 (2001).
[7] R. B. Bird, R. C. Armstrong, and O. Hassager, *Dynamics of Polymeric Liquids: Fluid Mechanics*, 2nd ed. (John Wiley & Sons, New York, 1987), Vols. 1 and 2.
[8] R. G. Larson, Instabilities in viscoelastic flows, Rheol. Acta **31**, 213 (1992).
[9] J. Azaiez and G. M. Homsy, Linear stability of free shear flow of viscoelastic liquids, J. Fluid Mech. **268**, 37 (1994).
[10] M. F. Hibberd, M. Kwade, and R. Scharf, Influence of drag reducing additives on the structure of turbulence in a mixing layer, Rheol. Acta **21**, 582 (1982).
[11] R. Scharf, Die Wirkung von Polymerzus itzen auf die Turbulenzstruktur in der ebenen Mischungsschicht zweier Stroeme, Rheol. Acta **24**, 272 (1985).
[12] J. M. Rallison and E. J. Hinch, Instabilty of a high-speed submerged elastic jet, J. Fluid Mech. **288**, 311 (1995).
[13] F. Sausset, O. Cadot, and S. Kumar, Experimental observation of frequency doubling in a viscoelastic mixing layer, C. R. Mecan. **332**, 1001 (2004).

[14] O. Cadot and M. Lebey, Shear instability inhibition in a cylinder wake by local injection of a viscoelastic fluid, Phys. Fluids **11**, 494 (1999).
[15] O. Cadot and S. Kumar, Experimental characterization of viscoelastic effects on two- and three-dimensional shear instabilities, J. Fluid Mech. **416**, 151 (2000).
[16] J. R. Cressman, Q. Baley, and W. I. Goldburg, Modification of a vortex street by a polymer additive, Phys. Fluids **13**, 867 (2001).
[17] P. K. Ray and T. A. Zaki, Absolute instability in viscoelastic mixing layer, Phys. Fluids **26**, 014103 (2014).
[18] A. Morozov (private communication).
[19] T. W. Searle, Ph.D. thesis, University of Edinburgh, Edinburgh, UK, 2018 (unpublished).
[20] A. N. Morozov and W. van Saarlos, An introductory essay on subcritical instabilities and the transition to turbulence in visco-elastic parallel shear flows, Phys. Rep. **447**, 112 (2007).
[21] A. Varshney and V. Steinberg, Elastic wake instabilities in a creeping flow between two obstacles, Phys. Rev. Fluids **2**, 051301(R) (2017).
[22] A. Groisman and V. Steinberg, Elastic turbulence in a polymer solution flow, Nature (London) **405**, 53 (2000).
[23] A. Groisman and V. Steinberg, Efficient mixing at low Reynolds numbers using polymer additives, Nature (London) **410**, 905 (2001).
[24] A. Groisman and V. Steinberg, Elastic turbulence in curvilinear flows of polymer solutions, New J. Phys. **6**, 29 (2004).
[25] Y. Liu, Y. Jun, and V. Steinberg, Concentration dependence of the longest relaxation times of dilute and semi-dilute polymer solutions, J. Rheol. **53**, 1069 (2009).
[26] W. Thielicke and E. Stamhuis, PIVlab—Towards user-friendly, affordable and accurate digital particle image velocimetry in MATLAB, J. Open Research Software **2**, e30 (2014).
[27] A lower value of Wi_{c1} found in this experiment compared with that reported in Ref. [21] can be explained by a different base for the ΔP measurements: In Ref. [21], ΔP was measured between the inlet with a narrow metal capillary inside the inlet tube and the tube location downstream from the second obstacle, whereas in the current experiment it is measured across the obstacles in the channel.
[28] Y. Jun and V. Steinberg, Power and Pressure Fluctuations in Elastic Turbulence Over a Wide Range of Polymer Concentrations, Phys. Rev. Lett. **102**, 124503 (2009).
[29] Y. Jun and V. Steinberg, Polymer concentration and properties of elastic turbulence in a swirling flow, Phys. Rev. Fluids **2**, 103301 (2017).
[30] A. Varshney and V. Steinberg, Drag enhancement and drag reduction in viscoelastic flow, Phys. Rev. Fluids (to be published).
[31] See Supplemental Material at http://link.aps.org/supplemental/10.1103/PhysRevFluids.3.103303 for movies and figures.
[32] A. Fouxon and V. Lebedev, Spectra of turbulence in dilute polymer solutions, Phys. Fluids **15**, 2060 (2003).
[33] T. Burghelea, E. Segre, and V. Steinberg, Elastic turbulence in von Karman swirling flow between two disks, Phys. Fluids **19**, 053104 (2007).
[34] Y. Jun and V. Steinberg, Elastic turbulence in a curvilinear channel flow, Phys. Rev. E **84**, 056325 (2011).
[35] J. Page and T. A. Zaki, The dynamics of spanwise vorticity perturbations in homogeneous viscoelastic shear flow, J. Fluid Mech. **777**, 327 (2015).